Making corrections to your proof

Please follow these instructions to mark changes or add notes to your proof. You can use Adobe Acrobat Reader (download the most recent version from **https://get.adobe.com**) or an open source PDF annotator.

For Adobe Reader, the tools you need to use are contained in **Annotations** in the **Comment** toolbar. You can also right-click on the text for several options. The most useful tools have been highlighted here. If you cannot make the desired change with the tools, please insert a sticky note describing the correction.

Please ensure all changes are visible via the 'Comments List' in the annotated PDF so that your corrections are not missed.

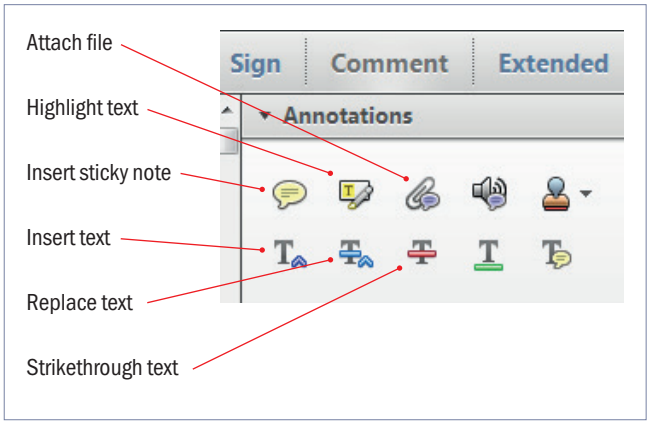

Do not attempt to directly edit the PDF file as changes will not be visible.

Replacing text

To replace text, highlight what you want to change then press the replace text icon, or right-click and press 'Add Note to Replace Text', then insert your text in the pop up box. Highlight the text and right click to style in bold, italic, superscript or subscript.

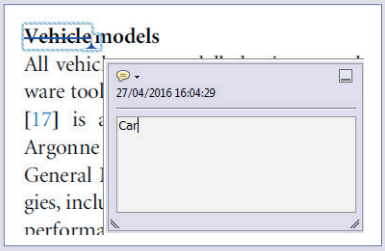

Inserting text

Place your cursor where you want to insert text, then press the insert text icon, or right-click and press 'Insert Text at Cursor', then insert your text in the pop up box. Highlight the text and right click to style in bold, italic, superscript or subscript.

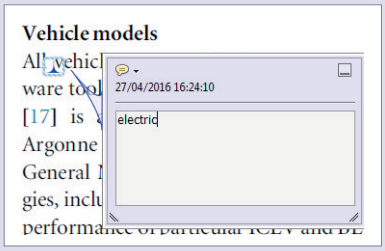

Deleting text

To delete text, highlight what you want to remove then press the strikethrough icon, or right-click and press 'Strikethrough Text'.

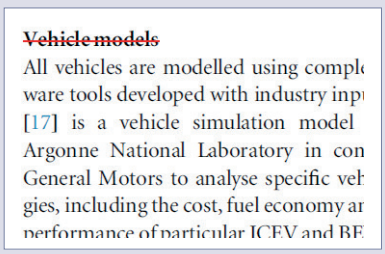

Highlighting text

To highlight text, with the cursor highlight the selected text then press the highlight text icon, or right-click and press 'Highlight text'. If you double click on this highlighted text you can add a comment.

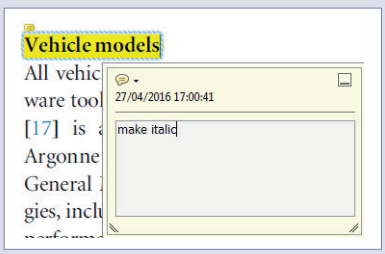

QUERY FORM

JOURNAL: Plasma Physics and Controlled Fusion

AUTHOR: F Pegoraro *et al*

TITLE: Coherent magnetic structures in self-organized plasmas

ARTICLE ID: ppcfab03b5

The layout of this article has not yet been finalized. Therefore this proof may contain columns that are not fully balanced/ matched or overlapping text in inline equations; these issues will be resolved once the final corrections have been incorporated.

Please check that the **names of all authors as displayed in the proof are correct**, and that all **authors are linked to the correct affiliations**. Please also confirm that the correct corresponding author has been indicated. **Note that this is your last opportunity to review and amend this information before your article is published**.

If an explicit acknowledgment of funding is required, please ensure that it is indicated in your article. If you already have an Acknowledgments section, please check that the information there is complete and correct.

SQ1
Please be aware that the colour figures in this article will only appear in colour in the online version. If you require colour in the printed journal and have not previously arranged it, please contact the Production Editor now.

We have been provided with ORCID iDs for the authors as below. Please confirm whether the numbers are correct.
F. Pegoraro 0000-0002-7216-5491
M. Veranda 0000-0002-5821-2896

Page 1

Q1
Please specify the corresponding author and provide his/her email address.

Page 5

Q2
Please check the edits made to the sentence 'In this picture…'.

Page 9

Q3
Please check the details for any journal references that do not have a link as they may contain some incorrect information. If any journal references do not have a link, please update with correct details and supply a Crossref DOI if available.

Page 9

Q4
Report references [11, 49] should contain author name, year, report title, report number and institution. Please provide the missing information.

Page 9

Q5
Publisher location and name are required for book reference [39]. Please provide the missing information.

APP Template V1.70 Article id: ppcfab03b5 Typesetter: MPS Date received by MPS: 04/02/2019 PE: MAC005961 CE: LE:

IOP Publishing Plasma Physics and Controlled Fusion

Plasma Phys. Control. Fusion **00** (2019) 000000 (9pp)

Coherent magnetic structures in self-organized plasmas

F Pegoraro[1], D Bonfiglio[2], S Cappello[2], G Di Giannatale[2], M V Falessi[3], D Grasso[4] and M Veranda[2]

[1] Dipartimento di Fisica, Pisa University, largo Pontecorvo 3, Pisa, Italy
[2] Consorzio RFX (CNR, ENEA, INFN, Università di Padova, Acciaierie Venete SpA) Corso Stati Uniti 4, Padova, Italy
[3] ENEA, Fusion and Nuclear Safety Department, C.R. Frascati, Via E. Fermi 45, Frascati (Roma), Italy
[4] ISC-CNR and Politecnico di Torino, Dipartimento Energia C.so Duca degli Abruzzi 24, Torino. Italy

Received 2 October 2018, revised 9 January 2019
Accepted for publication 31 January 2019
Published DD MM 2019

Abstract

Q1 The concept of Lagrangian coherent structures (LCS) has been recently applied to complex magnetic configurations in plasmas in order to find and characterize their main structural features. LCS make it possible to separate regions inside these configurations where field lines exhibit a different kind of behaviour. In the present article first we review the main features and uses of this technique and then apply it to the study of configurations that evolve into a self-organized quasi-single helicity state referring in particular to results obtained in the reversed-field pinch experiment in Padua.

Keywords: magnetized plasma, chaotic magnetic field, coherent structures, transport, self-organization

SQ1 (Some figures may appear in colour only in the online journal)

1. Introduction

The concept of Lagrangian coherent structures (LCS) was introduced in the context of transport processes in complex fluid flows, see [1]. In a two-dimensional configuration LCS correspond to special material lines which organize the flow, see e.g. [2] and for a review [3]. As highlighted in these references LCS provide a generalization to temporally aperiodic flows of the dynamical structures observed in autonomous and periodic systems, such as invariant manifolds, and separatethe flow domain into macro-regions inside which trajectories exhibit qualitatively different behaviour over the finite time span which characterize the LCS.

The LCS technique has been used to describe transport processes in a wide range of systems, as detailed e.g. in the Introduction of [4]. In [4, 5] LCS have been applied to the description of particle transport in magnetized plasmas using the magnetic field lines as a proxy for the structure of the particle trajectories. This specific application is the subject of the present article where we refer in particular to those laboratory plasma configurations, such as reversed-field pinches (RFPs), that are more subject to the onset of magnetic fluctuations and where the identification of the LCS and the study of their modification in different regimes is obviously of great physics interest. We recall that in [6] LCS have been used to show how applying boundary magnetic perturbations with different helicities gives rise to different transport barriers in a reversed pinch configuration. Here we investigate what kind of information the use of LCS can provide in the study of the magnetic field structure characterizing a self-organized, quasi-single helicity state in the RFP experiment in Padua. We note that the role of LCS in exposing a change of regime has also been stressed in different contexts e.g. in [7, 8]. In this latter reference it was noted in the context of the solar dynamo that the LCS in the velocity field and the related transport barriers 'suffer a dramatic change when the magnetic field undergoes the transition from a wave to an intermittent dynamo. The sharp contrast between the dynamics of LCS in these two dynamo regimes permits a unique analysis of the impact of the magnetic field on the velocity field, which provides an in-depth insight to the origin of intermittency in solar cycles.' More recently in a similar context it was shown in [9] that 'LCSs provide an accurate way of identifying transport barriers and kinematic and magnetic vortices in astrophysical turbulence' and it was remarked that 'these novel tools can improve monitoring and prediction of coronal

filament eruptions.' The present paper presents a short review of methods and results described in [4, 5], where the connection between LCS and the onset of magnetic stochasticity was investigated in a magnetized plasma in the presence of a large amplitude reconnection instability, and then extends the analysis of [6] regarding the role of LCS as indicators of a plasma transition into a self-organized quasi-single helicity state.

It is organized as follows. In section 2 the Hamiltonian nature of the magnetic field line equation and the relationship with the dynamics of one-dimensional non-autonomous dynamical systems, with the role of time taken by a coordinate along field lines, are recalled. In section 3 the use of the Poincaré sections and of the LCS is briefly reviewed. In section 4 we recall the definition of (hyperbolic) LCS. This section contains material already presented in previous publications but is needed in order to make the present review as self-contained as possible. In section 5 we briefly review the main results obtained in [4, 5] mostly with the aim of showing how the concept of magnetic field LCS as particle barrier can be extended to a magnetic configuration that varies in time and where particles with different velocities will experience different barriers. In section 6 we recall the physical context of the process of self-organization of the magnetic field configuration in simulations of the RFP in Padua. In section 7 we describe the numerical procedure adopted in order to find the LCS and show their structure before and after the plasma self-organization into a quasi-single helicity state. Finally conclusions are drawn in section 8.

2. Magnetic field as a Hamiltonian system

As is well known [10–15], due to their solenoidal nature, the field lines of a magnetic field in three-dimensional space that does not vanish within the domain of interest can be described as trajectories of a non-autonomous Hamiltonian system with one degree of freedom. The role of time is played by a spatial coordinate taken to label the points along a field line.

The equivalence between the magnetic field lines and the trajectories of non-autonomous Hamiltonian systems with one degree of freedom has been widely used in the literature by adopting the concepts that are proper of dynamical systems, see in particular [10, 16, 17].

For the RFP configuration considered in section 6 a convenient Hamiltonian representation can be obtained by using the so-called 'Boozer' coordinates, given by (ψ_t, θ, ζ) with ψ_t the toroidal flux (i.e. the flux of the magnetic field at constant toroidal angle ζ), θ the poloidal angle and ψ_p the poloidal flux:

$$\mathbf{B} = \nabla\psi_t \times \nabla\theta - \nabla\psi_p \times \nabla\zeta. \tag{1}$$

From the definition of magnetic field lines we obtain two equations in Hamiltonian form

$$\frac{\mathrm{d}\theta}{\mathrm{d}\zeta} = \frac{\mathbf{B}\cdot\nabla\theta}{\mathbf{B}\cdot\nabla\zeta} = \frac{\partial\psi_p}{\partial\psi_t}, \tag{2}$$

$$\frac{\mathrm{d}\psi_t}{\mathrm{d}\zeta} = \frac{\mathbf{B}\cdot\nabla\psi_t}{\mathbf{B}\cdot\nabla\zeta} = -\frac{\partial\psi_p}{\partial\theta}, \tag{3}$$

with $\psi_p(\psi_t, \theta, \zeta)$ the Hamiltonian, ψ_t the canonical momentum, θ the canonical coordinate, and ζ the 'time'. The choice of ζ as the time variable has been made in analogy to the one made in [4, 5] in order to allow for a direct comparison. We recall however that in the case of a RFP configuration this choice is only possible for $r < r_{\mathrm{rev}}$, i.e. in the region inside the radius r_{rev} where the toroidal field reverses. To integrate the field line equation in the whole domain, the toroidal flux ψ_t could be used as the Hamiltonian, with θ taking the role of time.

3. Poincaré sections and LCSs in non-autonomous dynamical systems with one degree of freedom

Non-autonomous periodic systems with one degree of freedom can be conveniently studied by means of the Poincaré section (stroboscopic map) method which makes it possible to reduce the dimensionality of the problem, see e.g. [18–20] and to reveal whether the motion of initial conditions is regular or chaotic. Furthermore, invariant manifolds of the map can be used to partition phase space into regions where trajectories have a qualitatively different behaviour on a given time-scale, e.g. bounded or unbounded [21–23]. These structures play a fundamental role in governing transport processes in non-autonomous dynamical systems and, in particular, they determine the so-called lobe dynamics [24–27]. Hyperbolic LCS instead, provide a different technique, based on the definition and identification of material lines that are characterized by their property of maximally attracting or repelling nearby material lines, which allows us to generalize these concepts to the study of dynamical systems defined over a finite amount of time without requiring their periodicity. This property of the LCS was exploited in [4, 5] in order to study the transport of particle in a magnetic configuration evolving in physical time and to ascertain how the appropriately defined LCS depend on the particle velocity and is briefly reviewed in section 5.

As indicated by the field line equations (2), (3), here we consider magnetic configurations that are periodic along the angle ζ that plays the role of the time. Although the Poincaré map can be used to study the system, the LCS technique makes it possible to further partition the regions characterized by chaotic trajectories into sub-domains where initial conditions have a qualitatively different behaviour on the time intervals which characterize the LCS. Therefore the calculation of the invariant manifolds is not required. We recall that as the time interval that defines the LCS increases these structures converge to the invariant manifolds mentioned above, see [3], and acquire their typical features.

4. Lagrangian coherent structures (LCS)

In this section we recall the definition of LCS that apply to a dynamical system (not necessarily Hamiltonian) in a 2D phase space $\boldsymbol{x}$ with continuous differentiable flow map

$$\boldsymbol{\phi}^t_{t_0}(\boldsymbol{x}_0) = \boldsymbol{x}(t, t_0, \boldsymbol{x}_0). \tag{4}$$

Two neighbouring points $\boldsymbol{x}_0$ and $\boldsymbol{x}_0 + \boldsymbol{\delta}x_0$ evolve into the points $\boldsymbol{x}$ and $\boldsymbol{x} + \boldsymbol{\delta}x$ under the linearized map

$$\boldsymbol{\delta}x = \boldsymbol{\nabla}\boldsymbol{\phi}^t_{t_0}\ \boldsymbol{\delta}x_0. \tag{5}$$

Given a curve $\gamma_0 = \{\boldsymbol{x}_0 = r(s)\}$ at each point $\boldsymbol{x}_0 \in \gamma_0$ we define the unit tangent vector $\boldsymbol{e}_0$ and the normal vector $\boldsymbol{n}_0$. In the time interval $[t_0, t]$ the dynamics of the system advects the *material line* γ_0 into γ_t and $\boldsymbol{x}_0 \in \gamma_0$ into $\boldsymbol{x}_t \in \gamma_t$. The linearized dynamics maps the tangent vector $\boldsymbol{e}_0$ into $\boldsymbol{e}_t$ which is tangent to γ_t and is given by

$$\boldsymbol{e}_t = \frac{\boldsymbol{\nabla}\boldsymbol{\phi}^t_{t_0}(\boldsymbol{x}_0)\boldsymbol{e}_0}{[\boldsymbol{e}_0\ \boldsymbol{C}^t_{t_0}(\boldsymbol{x}_0)\ \boldsymbol{e}_0]^{1/2}}, \tag{6}$$

where $\boldsymbol{C}^t_{t_0}(\boldsymbol{x}_0) \equiv (\boldsymbol{\nabla}\boldsymbol{\phi}^t_{t_0})^T\ \boldsymbol{\nabla}\boldsymbol{\phi}^t_{t_0}$ is the *Cauchy–Green strain tensor* and ^{T} stands for transposed. This symmetric tensor describes the deformation of an arbitrarily small circle of initial conditions, centred in $\boldsymbol{x}_0$ caused by the flow in a time interval $[t_0, t]$. Let $\boldsymbol{\xi}_{\max}$ and $\boldsymbol{\xi}_{\min}$ be the two eigenvectors of $\boldsymbol{C}^t_{t_0}(\boldsymbol{x}_0)$ corresponding to the real and positive eigenvalues $\lambda_{\max}$ and $\lambda_{\min}$. In the case of a Hamiltonian system phase space conservation implies that $\lambda_{\min}\ \lambda_{\max} = 1$. The curves with tangent vector along $\boldsymbol{\xi}_{\min}$ and, respectively, $\boldsymbol{\xi}_{\max}$ are called *strain lines* of the Cauchy–Green tensor. In general the mapping does not preserve the angle between vectors and therefore usually the normal vector $\boldsymbol{n}_t$ differs from $\boldsymbol{\nabla}\boldsymbol{\phi}^t_{t_0}\boldsymbol{n}_0$. Using the orthogonality condition $\boldsymbol{n}_0 \cdot \boldsymbol{e}_0 = \boldsymbol{n}_0\boldsymbol{\nabla}\boldsymbol{\phi}^{t_0}_t\boldsymbol{\nabla}\boldsymbol{\phi}^t_{t_0}\boldsymbol{e}_0 = 0$ and inserting equation (6) we obtain the expression for $\boldsymbol{n}_t$ which is given by

$$\boldsymbol{n}_t = \frac{(\boldsymbol{\nabla}\boldsymbol{\phi}^{t_0}_t)^T\boldsymbol{n}_0}{[\boldsymbol{n}_0\ \boldsymbol{C}^{-1}(\boldsymbol{x}_0)\ \boldsymbol{n}_0]^{1/2}}, \tag{7}$$

where $\boldsymbol{C}^{-1}(\boldsymbol{x}_0) = \boldsymbol{C}^{t_0}_t(\boldsymbol{x}_0)$ and the time interval marks have been suppressed as will be the case in the following formulae when not explicitly needed.

We define the *repulsion ratio* $\rho^t_{t_0}(\boldsymbol{x}_0, \boldsymbol{n}_0)$ as the ratio at which material points, in other words points advected by the flow, initially taken near the point $\boldsymbol{x}_0 \in \gamma_0$, increase their distance from the curve in the time interval $[t_0, t]$:

$$\rho^t_{t_0}(\boldsymbol{x}_0, \boldsymbol{n}_0) = \boldsymbol{n}_t\ \boldsymbol{\nabla}\boldsymbol{\phi}^t_{t_0}(\boldsymbol{x}_0)\ \boldsymbol{n}_0. \tag{8}$$

Using the previous definitions, $\rho^t_{t_0}(\boldsymbol{x}_0, n_0)$ can be expressed either in terms of n_0 or of n_t as

$$\begin{aligned}\rho^t_{t_0}(\boldsymbol{x}_0, n_0) &= [\boldsymbol{n}_0\ \boldsymbol{C}^{-1}(\boldsymbol{x}_0)\ \boldsymbol{n}_0]^{-1/2} \\ &= [\boldsymbol{n}_t\ \boldsymbol{C}(\boldsymbol{x}_0)\ \boldsymbol{n}_t]^{1/2}.\end{aligned} \tag{9}$$

Similarly, the *contraction rate* $L^t_{t_0}(\boldsymbol{x}_0)$ is proportional to the growth in time of the vector tangent to the material line

$$L(\boldsymbol{x}_0, \boldsymbol{e}_0) = [\boldsymbol{e}_0\ \boldsymbol{C}(\boldsymbol{x}_0)\ \boldsymbol{e}_0]^{1/2}. \tag{10}$$

4.1. LCS as maximal repulsion–attraction material lines

Here we adopt the definition of a Hyperbolic LCS as given in [2]. An LCS over a finite time interval $[t_0, t_0 + T]$ is defined as a line along which the repulsion rate is pointwise maximal. This leads, as shown in [2, 17], to the following definitions.

A line satisfying the following conditions at each point:

$$(a) \qquad \lambda_{\min} < \lambda_{\max}, \quad \lambda_{\max} > 1, \tag{11}$$

$$(b) \qquad \boldsymbol{e}_0 = \boldsymbol{\xi}_{\min} \tag{12}$$

the tangent vector is along the eigenvector associated with the smallest eigenvalue,

$$(c) \qquad \boldsymbol{\xi}_{\max} \cdot \boldsymbol{\nabla}\lambda_{\max} = 0 \tag{13}$$

the gradient of the largest eigenvalue is along the curve, is called a repulsive weak LCS (WLCS).

A WLCS which satisfies at each point the additional condition

$$\boldsymbol{\xi}_{\max}\ \cdot\ \boldsymbol{\nabla}^2\lambda_{\max}\ \cdot\ \boldsymbol{\xi}_{\max} < 0 \tag{14}$$

is called a repulsive LCS. Attractive LCS are defined as repulsive LCS of the backward time dynamics.

5. LCS in a reconnecting plasma

The system considered in this section is a sheared magnetic field configuration that is unstable to the onset of multiple-helicity magnetic field line reconnection. We assume the time evolution of the magnetic field to be given according to the numerical results presented in [28] and write

$$\mathbf{B} = B_0\mathbf{e}_z + \nabla\psi(x, y, z, t) \times \mathbf{e}_z. \tag{15}$$

For the sake of simplicity here, as in [4, 5], we consider a slab geometry with $\psi(x, y, z, t)$, x, z, y taking the roles of ψ_p, ψ_t/B_0, ζ, θ in equation (1) respectively. Specifically we take

$$\begin{aligned}\psi(x, y, z, t) = 0.19\cos(x) &\\ + \hat{\psi}_1(x, t)\cos(k_{1y}y + k_{1z}z) &\\ + \hat{\psi}_2(x, t)\cos(k_{2y}y + k_{2z}z) &\end{aligned} \tag{16}$$

in the domain $[-L_x, L_x] \times [-L_y, L_y] \times [-L_z, L_z]$ with $L_x = \pi$, $L_y = 2\pi$, $L_z = 16\pi$ with $k_{1y} = k_{2y} = 2\pi/L_y$ and $k_{1z} = 0$ while $k_{2z} = 2\pi/L_z$. Periodicity is assumed in all three directions. The initial perturbations, $\hat{\psi}_1(x, 0)$ and $\hat{\psi}_2(x, 0)$, are localized at the resonant surfaces $x_1 = 0$ and $x_2 = 0.71$ respectively.

At each fixed physical time t the magnetic flux function $\psi(x, y, z, t)$ plays the role of the Hamiltonian for the magnetic field lines with x and y canonical variables and z the magnetic Hamiltonian time.

In the linear phase two independent island chains are formed at their resonant surfaces. As the reconnection instability grows and the dynamics of the magnetic configuration becomes nonlinear, these chains expand. When they start to interact the regions where field lines are stochastic spread as discussed in [28]. In [4, 5] the LCS of this magnetic configuration were calculated at fixed t considering two

snapshots at $t = 415$, when chaos in the magnetic field lines has only started to develop, and at $t = 425$ when chaotic regions start to spread over the simulation domain. These configurations are periodic in the 'time variable' z. Additional details of the numerical technique adopted in order to compute the LCS are given in [5] together with the plots of the LCS. The technique used in [5] is based on the procedure described in [29].

Several conclusions were derived.

(a) It was shown explicitly that, although the Poincaré map provides a fundamental tool in order to study a 'time' periodic dynamical system, the LCS technique allows a more refined analysis since, as mentioned above, it makes it possible to further partition the regions characterized by a chaotic behaviour into sub-regions where trajectories have a qualitatively different behaviour on the time intervals which characterize the LCS.

(b) The robustness of the LCS as transport barriers was tested by performing a series of trajectory integration of magnetic field lines considering a set of initial conditions inside small neighbourhoods either of repelling or of attracting LCS and letting these trajectories evolve for $80L_z$. No flux through the LCS on the considered time span was observed unless regions close to lobes and tangles were considered as can be expected on the basis to the lobe dynamics briefly recalled in section III of In [4].

Subsequently in [4, 5], a trial was made in order to ascertain whether it was possible to account, at least in an approximate fashion, for the magnetic configuration change during the transit time of the plasma particle and to quantify the selective effect that this change can have on particles with different velocities. To keep the analysis as simple as possible a reduced model for the particle motion was used: the particle gyromotion and drifts were neglected and the particles dynamics was only included through their (constant) streaming velocity V along the guide field B_0. Therefore, a family of non-autonomous dynamical systems was introduced, characterized by a different velocity V, with Hamiltonian

$$\psi_V(x, y, z) \equiv \psi(x, y, z, t = (z - z_o)/V). \tag{17}$$

Such a Hamiltonian combines the physical time t and the magnetic configuration time z through the relation $t = (z - z_o)/V$ which specifies that the magnetic configuration must be adjourned as the particles move along the field lines. Again the details of how this method was implemented can be found in [4, 5] together with the plots of the LCS.

The main conclusions that were reached are:

(a) the obtained LCS differ significantly from the ones calculated at fixed time snapshots, making the V-dependent generalization worthwhile,

(b) particles with given velocities are characterized by specific LCS which, in general, are permeable to particles with different V;

(c) attracting LCS play a special role, as mentioned already by Haller [30] when introducing the concept of 'skeleton of the flow', since particles tend to arrange themselves along these curves.

Finally it was stressed that *per se* the LCS method is applicable without approximations of the particle motion by referring to the full particle dynamics in 3D coordinate space and by employing e.g. the exact particle Hamiltonian in time varying electromagnetic fields. However the simplified model of [4, 5] is valuable as it provides results that are easy to visualize and as it avoids the use of higher dimensionality plots by resorting a one-dimensional set of models characterized by the single parameter V.

6. Self-organized RFP configurations

The self-organization process into a global magnetic helical structure has been shown to be a characteristic feature of the plasma dynamics in RFP. This was shown first within 3D nonlinear magnetofluid numerical simulations [31], and it was then observed in high current RFP experiments [32, 33]. This self-organization process is identified with the nonlinear saturation of a single MHD instability [34] which breaks the toroidal axisymmetry, forces the magnetic field lines to wind around a single helical axis and impose a quasi-2D symmetry. This phenomenon allows the chaos, naturally induced by the overlapping of the various magnetic islands associated with the secondary MHD instabilities, to be healed. This brings beneficial effects in terms of increased plasma temperature in the helical core of the plasma, measured in experiments [35].

In the present section we recall the numerical MHD model and the numerical simulations through which these data, describing the establishment of a helical symmetry, are obtained. Then in sections 7.2 and 7.4 we will compute the LCS and describe their structure in two important moments of the plasma evolution: shortly before and soon after the establishment of the helical symmetry.

6.1. MHD model

The following set of dimensionless visco-resistive MHD equations [31, 36]

$$\frac{\partial \boldsymbol{v}}{\partial t} + \boldsymbol{v} \cdot \nabla \boldsymbol{v} = \boldsymbol{J} \times \boldsymbol{B} + \nu \nabla^2 \boldsymbol{v}, \tag{18}$$

$$\frac{\partial \boldsymbol{B}}{\partial t} = \nabla \times (\boldsymbol{v} \times \boldsymbol{B} - \eta \boldsymbol{J}), \tag{19}$$

$$\nabla \times \boldsymbol{B} = \boldsymbol{J}, \qquad \nabla \cdot \boldsymbol{B} = 0, \tag{20}$$

is solved numerically in cylindrical geometry. Here $\boldsymbol{v}$ represent the velocity field, $\boldsymbol{B}$ is the magnetic field and $\boldsymbol{J}$ is the current density. The dimensionless plasma resistivity is denoted by η, while ν indicates the plasma viscosity. Although the plasma pressure is neglected, this model has been shown in [37] to capture the major physical effects observed in RFP's. In addition it predicted alternative helical magnetic configurations, then observed in the RFX-mod experiment in Padua, that can be obtained by helically modulating the boundary conditions of the radial component of the magnetic field [6, 38].

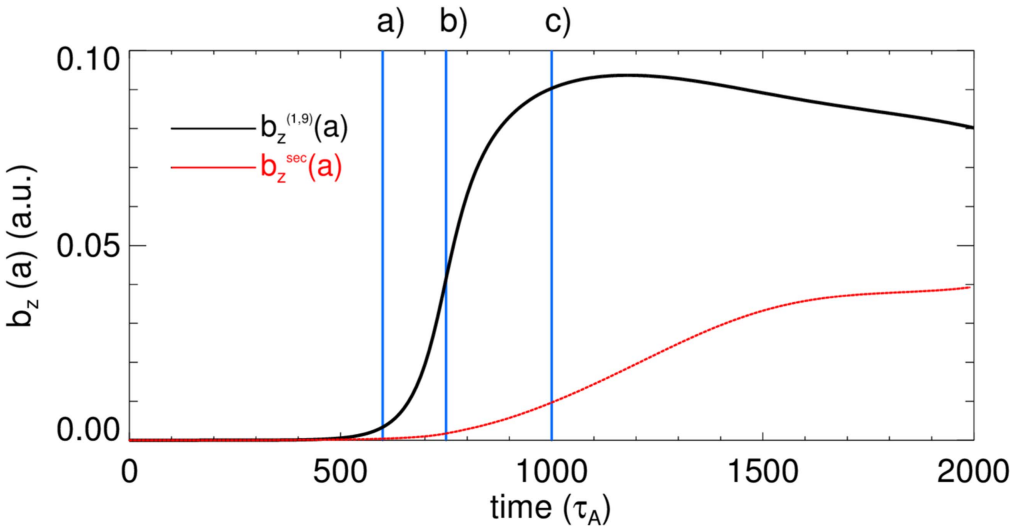

Figure 1. Temporal evolution of the axial component of the magnetic field associated with the dominant mode at the plasma edge (continuous black line). Temporal evolution of the $m = 1$ secondary modes is plotted with a red line. The first two blue vertical lines indicate the time of the two snapshots used in the calculation of the Lagrangian coherent structures, shown in figures 2 and 5 respectively before and after the formation of the quasi-helical state. The third vertical blue line at $t = 1000\,\tau_A$ describe a snapshot in which the chaos healing process is completed.

6.2. Numerical setup

Equations (18)–(20) are solved in a cylindrical geometry (r, θ, z) with aspect ratio $R_0/a = 4$, where $a = 1$ is the cylinder radius and $2\pi R_0$ the periodicity of the cylinder in the axial direction. Resistivity increases towards the edge while viscosity is uniform. The magnetic Lundquist number $S = \tau_R/\tau_A = 3 \times 10^4$, while the viscous Lundquist number, $M = \tau_\nu/\tau_A = 3 \times 10^1$, here τ_A is the Alfvén time and τ_R, τ_ν are the resistive and viscous time scales respectively. The boundary conditions are no-slip for the velocity field (i.e. $v_\theta(a) = v_z(a) = 0$) and ideal wall for the magnetic field (i.e. $B_r(a) = 0$). The equations are Fourier-transformed in the poloidal and in the axial directions with m for the poloidal number and n the axial number.

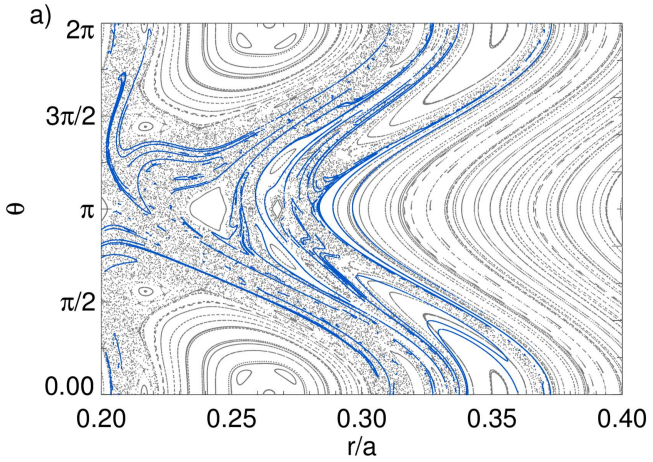

Figure 2. Poincaré map and LCS of the magnetic configuration corresponding to the snapshot taken at $t = 600\,\tau_A$, i.e. before the formation of the quasi-helical state. LCS are overplotted in blue. In this picture we show only the relevant radial region around the $m = 1$, $n = 9$ helical core (at $r = 0.26a$, $\theta = 0$), where a weakly chaotic magnetic field is present.

6.3. Magnetic field dynamics

The numerical simulation is initiated from an axis-symmetric, unstable equilibrium, with pinch parameter $\Theta = B_\theta(a)/\langle B_z\rangle = 1.6$, that is slightly perturbed. In a first stage, around $t = 600\,\tau_A$ (first vertical blue line in figure 1), only two relevant MHD modes are present, corresponding to those with the highest growth rate. The largest one has $m = 1$ and $n = 9$, meaning that it creates a structure of islands winding nine times around the axis of the cylinder. The other mode has $m = 1$ and $n = 10$. Despite their small amplitude at $t = 600\,\tau_A$, the magnetic islands associated to the modes interact and a macroscopic chaotic region appears between them (see figure 2).

As the plasma dynamics evolves, the islands grow increasing the region characterized by chaotic magnetic field lines. At $t = 750\,\tau_A$ (second vertical blue line in figure 1), the amplitude of the $m = 1$, $n = 9$ mode becomes so large that the effect of secondary perturbations is negligible and the mode can impress its helical symmetry to the whole configuration.

After $t = 790\,\tau_A$, chaos is strongly reduced in the whole domain, as the $m = 1$, $n = 9$ mode remains the dominant one, as can be seen in figures 5 and 6. Interestingly, though the intensity of the secondary perturbations to the helical state continues to increase after $t = 750\,\tau_A$ (see red line in figure 1), a magnetic chaos healing process occurs despite the presence of remnant spurious modes, contrary to a naïve application of Chirikov criterion [39] reading 'the larger the amplitudes and the number of Fourier components, the more chaotic the dynamics'. A more detailed description of this simulation can be found in [40].

7. LCS in the self organizing RFP configuration

In this section we apply the definition of the LCS given in sections 4 and 4.1 to the snapshots, taken at $t = 600\ \tau_A$ and at $t = 750\ \tau_A$ of the evolving RFP magnetic configuration as illustrated in figure 1. First we describe the numerical algorithm used and then we discuss the effects of the transition to the quasi-single helicity state on the LCS.

7.1. Algorithm description

In order to compute the LCS, the numerical algorithm requires a grid of initial conditions and the evolution of such initial conditions under the action of a vector field for a time span T. These data are then used to compute the gradient of the flow map $\phi_{t_0}^T$ in equation (4). Once this matrix is obtained, it is straightforward to compute the Cauchy–Green tensor defined below equation (6) and its eigenvalues ($\lambda_{\min}$, $\lambda_{\max}$) and eigenvectors ($\boldsymbol{\xi}_{\min}$, $\boldsymbol{\xi}_{\max}$) (additional details on the computation of the Cauchy–Green tensor in a general curvilinear geometry are given in the appendix). Finally, it is possible to construct curves that follow the eigenvectors and to evaluate whether they are or not LCSs by inspecting the validity of the conditions given in section 4.1. However, trying to compute the LCS over the whole domain is numerically too demanding. As shown in [29], a convenient strategy is based on the calculation of the local maxima of the finite time Lyapunov exponents (FTLE) field σ, defined as

$$\sigma(\boldsymbol{x}_0,\, t_0,\, t) = \frac{1}{2|t - t_0|} \ln \lambda_{\max}(\boldsymbol{x}_0,\, t_0,\, t) \tag{21}$$

and the use of the points where the local maxima of the FTLE field are located as the starting points for the integration along the eigenvectors.

The integration of the curves defined by the tangent vector given by equation (12), with initial conditions given by previously selected maxima of the FTLE field, is performed by using a fourth order Runge–Kutta method.

After the integration, we check whether the curves we have obtained satisfy equations (13), (14). Equation (13) is the most delicate to verify because most LCSs lie along the ridges of the FTLE field (21) where the gradients of the FTLE field are difficult to compute numerically. Therefore we relax this condition and, instead of $\boldsymbol{\xi}_{\max} \cdot \boldsymbol{\nabla}\lambda_{\max} = 0$ we impose $\boldsymbol{\xi}_{\min} \times \boldsymbol{\nabla}\lambda_{\max} = 0$. These two conditions are equivalent since the eigenvectors of the Cauchy–Green tensor are orthogonal. Actually at each point $\mathbf{r}_i$ along the integrated curve we require that $||\boldsymbol{\xi}_{\min}(\boldsymbol{r}_i) \times \boldsymbol{\nabla}\lambda_{\max}|| \leqslant \mathcal{T}$ where $\mathcal{T}$ is an acceptance threshold. If a point does not fulfil this condition we explore the neighbouring grid points to check whether we are indeed very close to a ridge where the quantity $\nabla\lambda$ may change suddenly direction. The above procedure allows us to find WLCSs, as defined below equation (12). We can further restrict the search of the LCS by applying the condition given by equation (14) which ensures that the selected curve is the most repelling material line among neighbouring material lines (for additional details see [17]).

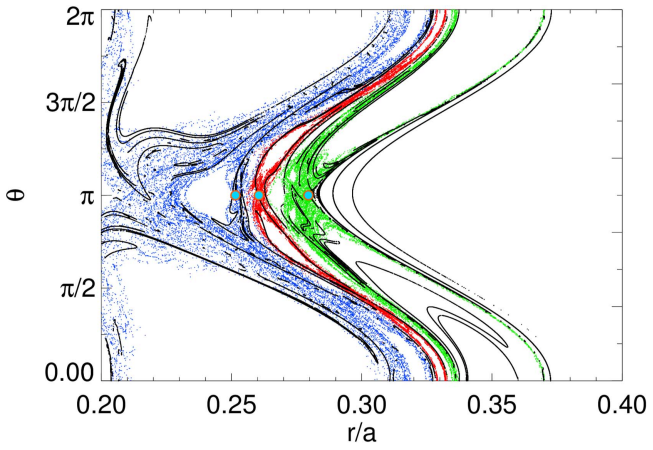

Figure 3. Evidence that LCS divide the space in separated regions. Initial conditions blue dots separated by a LCS remain separated for a finite amount of time.

7.2. LCS before the formation of the quasi-helical state

An investigation of the structure of the magnetic configuration at $t = 600\,\tau_A$,before the formation of the quasi-helical state, has been already presented in [41] in terms of a different definition of LCS (see [42]) based on the so-called 'second derivative ridges' of the FTLE field in equation (21). For a discussion of the difference between the two definitions, and of the shortcomings of the definition in terms of the ridges of the FTLE field, see e.g. Section V of [4]. As a difference from the case shown in [41] we adopt the definition of the LCS given in section 4 and compute them with the algorithm, described above in section 7.1 and analyse the differences in the results. To do so, first we consider the Poincaré map and the LCS for the magnetic configuration corresponding to the snapshot at $t = 600\tau_A$, figure 2. We observe that the LCS structures in figure 2 emanate from hyperbolic points: some of them surround the magnetic islands, separating the chaotic region from a regular one, while others are found in the chaotic region of the magnetic field. We focus on these ones, and show, in figure 3, that they provide a sharp division between a series of separate regions that cannot be easily located by inspecting the Poincaré plot. In the figure we show that magnetic field lines starting at the opposite sides of an LCS remain separated, at least for a finite time $\bar{\tau}$ (here corresponding to ∼100 toroidal turns), which is much longer than the dynamical scale (measured by the Alfvèn time, $\bar{\tau}/\tau_A \sim 10^3$) and longer than the collisional time scales (measured by the electron–ion collision time $\bar{\tau}/\tau_{ei} \sim 10^1$). Thus LCS mark in a clear way barriers to the transport of magnetic field lines. The results shown here and in [41, 6] indicate that LCSs may provide a good candidate to explain the formation of electron internal transport barriers observed in the RFP experiment in Padua (RFX-mod device) [43, 38, 35].

We note here that in figures 2 and 3 we plotted, for graphical simplicity, only repulsive LCS, while the attractive ones, which have a similar structure, are not shown. A comparison with the results published in [41] shows that the two methods individuate coherent structures with different

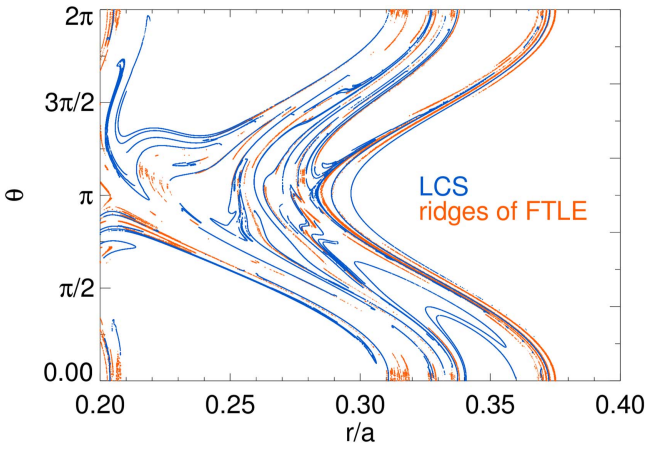

Figure 4. Comparison between the structure of repelling LCS in blue (the same as the ones in figure 3) and the ridges of the FTLE in orange (same as computed in figure 7 of [46]). They are qualitatively similar but LCS offer a deepest insight of the topological structure of coherent structures.

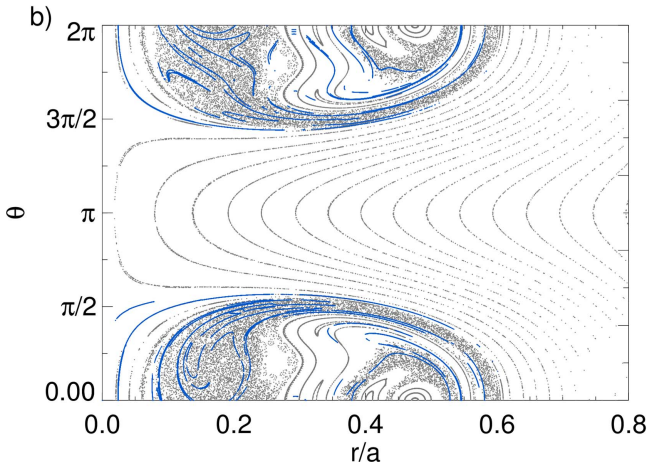

Figure 5. Poincaré map and LCS of the magnetic configuration corresponding to the snapshot taken at $t = 750\,\tau_A$, i.e. after the formation of the quasi-helical state. One can notice that the O-point of the magnetic island, located at $r = 0.26a$ in figure 2, now is the only O-point in the whole domain (helical self-organization). LCS are overplotted in blue. In this picture we show a wider radial region than in the plot of figure 2, because the helical region occupies a larger plasma volume.

precision. The algorithm described in section 7.1 detects more continuous structures due to the fact that the curves that define the LCS are here integrated following the eigenvector field, defined in the whole space by equation (12), while in the previous work coherent structures were computed as second derivative ridges of the FTLE field defined in equation (21), which could not always be found in a continuous manner. Furthermore, a comparison between figure 7 in [41] and figure 2 shows that the new algorithm can detect finer LCS. With the new algorithm we can also observe the LCS associated with the separatrix of the dominant $m = 1$, $n = 9$ magnetic island: in particular the one near $r = 0.21a$, $\theta \sim 5/4\pi$ in figure 2 shows the typical lobe structure [44, 45].

7.3. Relationship between ridges and LCS

A brief comparison between two methods for computing coherent structures can be performed. The first method is described in [41], and is based on the computation of second derivative ridges of the FTLE field, defined in equation (21). The second method is the one described in section 7.1 of this paper, and is based on the computation of the most repelling/attracting material lines. A direct superposition of the structures found by the two methods can be observed in figure 4.

Visual comparison shows that the two methods are in good general agreement, and identify coherent structures with different precision. The new algorithm described in this paper detects more continuous structures due to the fact that the curves that define the LCS are integrated following the eigenvector field, defined in the whole space by equation (12), while in the previous work coherent structures could not always be found in a continuous manner due to the Eulerian approach of the calculations. Furthermore, the comparison of figure 4 shows that the new algorithm can detect finer LCS. With the new algorithm we can also observe the LCS associated with the separatrix of the dominant $m = 1$, $n = 9$ magnetic island: in particular the one near $r = 0.21\,a$, $\pi \lesssim \theta \lesssim 5/4\pi$ in figure 2 shows the typical lobe structure [44, 45], or the similar lobe structure, associated to the $m = 1$, $n = 10$ magnetic island, observed near $r = 0.28a$, $\theta \sim 3/4\pi$.

7.4. LCS after the formation of the quasi-helical state

In figure 5 we consider the magnetic field configuration at $t = 750\,\tau_A$, right after the formation of the helical state i.e. after the O-point of the magnetic island associated to the $m = 1$, $n = 9$ mode (at $r = 0.26a$, $\theta = 0$ in figure 2) becomes the main O-point of the helical state. At this time there are no hyperbolic LCS in the region $\pi/2 < \theta < 3\pi/2$, while residual LCS are present only in the chaotic region surrounding the O-point (now at $r = 0.5a$, $\theta = 0$) of the $m = 1$, $n = 9$ helical structure which is responsible for the healing of magnetic chaos shown at $t = 600\,\tau_A$ in figure 2.

Obviously, in the region where the Poincaré map exhibits a regular behaviour there is no need to compute the LCS. At $t = 750\ \tau_A$ the pattern is very different since the separatrix of the dominant mode disappears into the new global helical state, a major topological change linked, in the experiments, to beneficial transport properties [35].

At $t = 1000\,\tau_A$ the process of magnetic chaos healing is complete, as can be seen observing the Poincaré plot in figure 6, characterized by the presence of well conserved magnetic flux surfaces that can be simply described in terms a one-dimensional helical flux function χ. The helical flux function can be defined by the equation $\boldsymbol{B} \cdot \nabla\chi = 0$. For the magnetic field here analysed, characterized by a $h = n/$

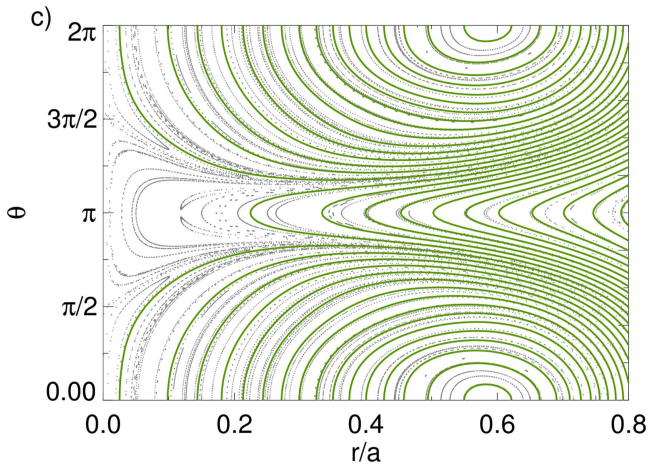

Figure 6. Poincaré map (in grey) of the magnetic configuration corresponding to the snapshot taken at $t = 1000\,\tau_A$, i.e. well after of the quasi-helical state. An LCS computation is not relevant in this case, because the helically symmetric magnetic field can be described in a simpler way by the helical flux function χ, defined in equation (22). The constant χ surfaces are plotted in green.

$m = 9$ helical symmetry in cylindrical geometry we find:

$$\chi(r,\,\theta,\,z) = A_z^{0,0}(r) + \frac{h}{R_0}A_\theta^{0,0}(r) + \sum_m\left(A_z^{m,hm}(r) + \frac{h}{R_0}A_\theta^{m,hm}(r)\right)\mathrm{e}^{\mathrm{i}(m\theta+hz/R_0)}, \qquad (22)$$

with $\boldsymbol{A}$ the vector potential associated with the magnetic field by $\boldsymbol{B} = \nabla \times \boldsymbol{A}$ (we choose $A_r = 0$ as a gauge). Constant χ surfaces, coloured in green in figure 6, describe correctly the Poincarè plot of the helically symmetric field (in grey).

8. Conclusions

LCS represent a very convenient tool that makes it possible to identify within a complex magnetic configuration macro-regions distinguished by a qualitatively different behaviour of the magnetic field lines.

In this work the concept of LCS is briefly reviewed and applied to magnetic configurations describing the phenomenon of 'transition from stochasticity to order', a typical feature of complex systems, where they can be most useful.

The analysis performed in [4, 5], here briefly reviewed, has shown in detail how this technique can be fruitfully applied to the study of the growing level of chaoticity in a magnetic configuration with two partly overlapping island chains and have related this process to the modification of the transport of the plasma particles. In addition it has been shown that it is possible through a simplified model to account for the evolution of the magnetic configuration during the transit time of the plasma particle through the magnetic configuration and to quantify the selective effect that this change can have on the transport of particles with different velocities.

In the present article the LCS technique has been specifically applied to a RFP configuration that undergoes a process of self-organization and reduction of magnetic chaoticity due to the establishment of a quasi-single helicity state. Following these results and the ones in [6] we see that on the one hand LCS correctly describe the separation between non communicating regions inside a stochastic magnetic field where the high gradients observed in the electron temperature profiles in RFP machines can be located and on the other hand that the rearrangement of the LCS represents a powerful monitor for the changes brought to the plasma dynamics by the magnetic field self-organization into a quasi-helical state, greatly improving the insights offered by other inspections methods like Poincaré sections. This last result shows that LCS can provide important insight into the transition of a wide range of physical systems from a chaotic to a self-organized state: an example referring to a change of regime on the solar dynamo from a wave ragime to an intermittent regime [9] was already mentioned in the text. Actually the process of emergence of self-organized features represents an essential feature of complex systems and occurs in different physical systems as exemplified for fluids by the Bénard rolls [47] formed in the presence of thermal convection, see in particular [48], or by vortices in atmosphere of Jupiter [49].

Appendix

We compute the gradient of the flow map $\boldsymbol{\phi} = \phi^i \mathbf{e}_i$ in a general geometry, with coordinates u^i and $\mathbf{e}^i$ and $\mathbf{e}_i$ the contravariant and covariant basis vectors, in the tensor form

$$\frac{\partial}{\partial u^i}\{\phi^j \mathbf{e}_j\} \otimes \mathbf{e}^i = A^k{}_\ell\ \mathbf{e}_k \mathbf{e}^\ell = \mathcal{A}^k{}_\ell \hat{e}_k \hat{e}^\ell, \qquad (23)$$

where summation over repeated indices is understood and in the last equality the unitary basis vectors $\hat{e}^i = \mathbf{e}^i/\|\mathbf{e}^i\|$ and $\hat{e}_i = \mathbf{e}_i/\|\mathbf{e}_i\|$ have been used. Writing the transpose of $\mathcal{A}$ as $\mathcal{A}^T = \mathcal{B}^m{}_k \hat{e}_m \hat{e}^k$, the Cauchy–Green tensor becomes

$$\mathcal{C}^m_j \hat{e}_m \hat{e}^j = \mathcal{B}^m{}_k \mathcal{A}^k{}_j \hat{e}_m \hat{e}^j. \qquad (24)$$

Then we specialize equation (23) to a cylindrical geometry which is the one used in the Specyl and NEMATO numerical runs reported in section 6.2 and compute the eigenvectors of the Cauchy–Green tensor as $\boldsymbol{\xi} = \xi_r \hat{e}_r + \xi_\theta \hat{e}_\theta$ (we recall that in cylindrical geometry $\hat{e}_i = \hat{e}^i$). Finally, we solve the differential equation

$$\mathrm{d}\mathbf{l}/\mathrm{d}s = \boldsymbol{\xi}(\mathbf{r}),\ \rightarrow \mathrm{d}r/\mathrm{d}s = \xi_r,\ \ \mathrm{d}\theta/\mathrm{d}s = \xi_\theta/r \qquad (25)$$

in a logical grid built as $(r,\,\theta) \rightarrow (x_{\mathrm{idx}},\,y_{\mathrm{idx}})$, where $r = r_0 + \Delta r\ x_{\mathrm{idx}}$, $\theta = \theta_0 + \Delta\theta\ y_{\mathrm{idx}}$ and $\Delta r = 1/N_r$, $\Delta\theta = 2\pi/N_\theta$ with N_θ, and N_r the number of mesh points inside the simulation domain $0 \leqslant \theta \leqslant 2\pi$ and $0.20 \leqslant r/a \leqslant 0.45$. In the case of the LCS in figure 2 we took $N_\theta = 8400$, and $N_r = 4096$.

ORCID iDs

F Pegoraro https://orcid.org/0000-0002-7216-5491

M Veranda https://orcid.org/0000-0002-5821-2896

References

[1] Haller G and Yuan G 2000 *Physica* D **147** 352–70
[2] Haller G 2011 *Physica* D **240** 574–98
[3] Haller G 2015 *Ann. Rev. Fluid Mech.* **47** 137–62
[4] Di Giannatale G, Falessi M V, Grasso D, Pegoraro F and Schep T 2018 *Phys. Plasmas* **25** 052306
[5] Di Giannatale G, Falessi M V, Grasso D, Pegoraro F and Schep T 2018 *Phys. Plasmas* **25** 052307
[6] Veranda M *et al* 2017 *Nucl. Fusion* **57** 116029
[7] Carlevaro N, Falessi M V, Montani G and Zonca F 2015 *J. Plasma Phys.* **81** 495810515
[8] Chian A C L, Brandenburg A, Proctor M R E and Rempel E L 2012 *EGU Gen. Assem. Conf. Abstracts* **14** 2444
[9] Chian A C L, Miranda R A, Rempel E L and Schmieder B 2018 *Proc. Int. Astron. Union* **13** 285–8
[10] Cary J R and Littlejohn R G 1983 *Ann. Phys.* **151** 1–34
[11] Kruskal M D 1952 Some properties of rotational transforms
Q4 *Tech. rep.* Forrestal Research Center, Princeton University
[12] Kerst D 1962 *J. Nucl. Energy* C **4** 253
[13] Gelfand I, Morozov A, Sololev L, Graev M and Zueva N 1962 *Sov. Phys.—Tech. Phys.* **6** 852
[14] Morozov A and Solov'ev L 1966 *Rev. Plasma Phys.* **2** 1
[15] Boozer A H 1981 *Phys. Fluids* **24** 1999–2003
[16] Borgogno D, Grasso D, Pegoraro F and Schep T 2011 *Phys. Plasmas* **18** 102307
[17] Falessi M V, Pegoraro F and Schep T 2015 *J. Plasma Phys.* **81** 495810505
[18] Arnold V I, Kozlov V V and Neishtadt A I 2007 *Mathematical Aspects of Classical and Celestial Mechanics* vol 3 (Berlin: Springer Science & Business Media)
[19] Wiggins S 1992 *NASA STI/Recon Tech. Rep.* A **92** 28228
[20] Vulpiani A 2010 *Chaos: from Simple Models to Complex Systems* vol 17 (Singapore: World Scientific)
[21] Mackay R S, Meiss J and Percival I 1987 *Physica* D **27** 1–20
[22] Meiss J 2015 *Chaos* **25** 097602
[23] Ottino J M 1989 *The Kinematics of Mixing: Stretching, Chaos, and Transport* vol 3 (Cambridge: Cambridge University Press)
[24] Wiggins S 2013 *Chaotic Transport in Dynamical Systems* vol 2 (New York: Springer Science & Business Media)
[25] Rom-Kedar V and Wiggins S 1990 *Arch. Ration. Mech. Anal.* **109** 239–98
[26] Rom-Kedar V, Leonard A and Wiggins S 1990 *J. Fluid Mech.* **214** 347–94
[27] Malhotra N and Wiggins S 1998 *J. Nonlinear Sci.* **8** 401–56
[28] Borgogno D, Grasso D, Porcelli F, Califano F, Pegoraro F and Farina D 2005 *Phys. Plasmas* **12** 032309
[29] Onu K, Huhn F and Haller G 2015 *J. Comput. Sci.* **7** 26–36
[30] Peacock T and Haller G 2013 *Phys. Today* **66** 41
[31] Cappello S and Biskamp D 1996 *Nucl. Fusion* **36** 571–81
[32] Escande D F *et al* 2000 *Phys. Rev. Lett.* **85** 1662–5
[33] Martin P *et al* 2003 *Nucl. Fusion* **43** 1855
[34] Escande D, Paccagnella R, Cappello S, Marchetto C and D'Angelo F 2000 *Phys. Rev. Lett.* **85** 3169
[35] Lorenzini R *et al* 2009 *Nat. Phys.* **5** 570
[36] Cappello S 2004 *Plasma Phys. Control. Fusion* **46** B313
[37] Bonfiglio D, Veranda M, Cappello S, Escande D F and Chacón L 2013 *Phys. Rev. Lett.* **111** 085002
[38] Piovesan P *et al* 2009 *Nucl. Fusion* **49** 085036
[39] Lichtenberg A and Lieberman M 1992 *Regular and Chaotic* Q5
Dynamics 2nd edn (Springer Science)
[40] Bonfiglio D, Veranda M, Cappello S, Chacón L and Spizzo G 2010 *J. Phys.: Conf. Ser.* **260** 012003
[41] Rubino G, Borgogno D, Veranda M, Bonfiglio D, Cappello S and Grasso D 2015 *Plasma Phys. Control. Fusion* **57** 085004
[42] Shadden S C, Lekien F and Marsden J E 2005 *Physica* D **212** 271–304
[43] Sonato P *et al* 2003 *Fusion Eng. Des.* **66** 161
[44] Evans T E, Roeder R K W, Carter J A and Rapoport B I 2004 *Contrib. Plasma Phys.* **44** 235–40
[45] Punjabi A and Boozer A 2014 *Phys. Lett.* A **378** 2410–6
[46] Rubino G, Borgogno D, Veranda M, Bonfiglio D, Cappello S and Grasso D 2015 *Plasma Phys. Control. Fusion* **57** 085004
[47] Chandrasekhar S 1982 *Hydrodynamic and Hydromagnetic Stability* (New York: Dover)
[48] Sugawara T, Yoshimura and Hiroaki 2012 *The Proc. of Mechanical Engineering Congress (Japan)* 052014
[49] Hadjighasem A and Haller G 2013 *Oberwolfach Reports A* pp 238–40